





Exact mobility edges in the non-Hermitian t_1 - t_2 model: Theory and possible experimental realizations

Xu Xia ¹, Ke Huang ², Shubo Wang ², and Xiao Li ^{2,3,*}

¹*Chern Institute of Mathematics and LPMC, Nankai University, Tianjin 300071, China*

²*Department of Physics, City University of Hong Kong, Kowloon, Hong Kong SAR, China*

³*City University of Hong Kong Shenzhen Research Institute, Shenzhen 518057, Guangdong, China*



(Received 4 June 2021; revised 1 January 2022; accepted 19 January 2022; published 31 January 2022)

Quantum localization in 1D non-Hermitian systems, especially the search for exact single-particle mobility edges, has attracted considerable interest recently. While much progress has been made, the available methods to determine the ME in such models are still limited. In this work, we use a new method to find a new class of exact mobility edges in 1D non-Hermitian quasiperiodic models with parity-time (\mathcal{PT}) symmetry. We illustrate our method by studying a specific model. We first use our method to determine the energy-dependent mobility edge as well as the spectrum for localized eigenstates in this model. We then demonstrate that the metal-insulator transition must occur simultaneously with the spontaneous \mathcal{PT} -symmetry breaking transition in this model. Finally, we propose an experimental protocol based on a 1D photonic lattice to distinguish the extended and localized single-particle states in our model. The results in our work can be applied to studying other non-Hermitian quasiperiodic models.

DOI: [10.1103/PhysRevB.105.014207](https://doi.org/10.1103/PhysRevB.105.014207)

I. INTRODUCTION

Quantum localization in disordered media has been a central topic in condensed matter physics since the seminal work by P. W. Anderson in 1958 [1]. In particular, while an infinitesimal amount of disorder will localize all eigenstates in 1D and 2D systems, the full localization transition in 3D systems will only occur at a finite disorder strength [2–4]. At weaker disorders, however, localized and extended eigenstates in 3D systems can coexist in the energy spectrum, leading to the appearance of a mobility edge (ME).

Recently, quasiperiodic systems have emerged as a viable alternative platform to study quantum localization in the experiment, partly because they are much easier to realize than those with random disorders. Importantly, they have been widely used in the experimental investigation of many-body localization (MBL) in 1D and 2D systems [5–11]. Moreover, the existence of ME in 1D quasiperiodic systems has also been studied extensively in theory [12–26]. Such efforts culminated in the recent experimental observation of ME in various 1D systems [27–32].

Meanwhile, Anderson localization in non-Hermitian systems [33–51], especially the existence of ME in such systems [52–59], have attracted considerable interest recently. In particular, much attention has been devoted to systems with the parity-time symmetry (\mathcal{PT} symmetry). This symmetry allows for an entirely real energy spectrum when the non-Hermitian parameter λ is below a critical value λ_c ; only when $\lambda > \lambda_c$ complex energies emerge in the spectrum [60–62]. In addition, several properties unique to non-Hermitian systems

have also been identified, such as the non-Hermitian skin effects and the existence of exceptional points. However, several critical open questions still remain open in this field. Notably, most existing work determines the exact ME in a non-Hermitian model using self-duality relations, similar to what has been done in their Hermitian counterparts. As a result, when we turn off the non-Hermitian parameter, the model is still known to have an exact ME. Can we develop a new method to determine the expression of ME in order to circumvent this limit? Crucially, is it possible that a non-Hermitian quasiperiodic model carries an exact ME while its Hermitian counterpart is not known to have one? Another critical question is that the existence of ME in a non-Hermitian system has not been experimentally established yet. This is partially due to the fact that models with exact MEs are difficult to construct, and thus they often involve a complicated hopping structure or fine-tuned onsite potentials. Thus a non-Hermitian model that can be easily implemented in the experiments is highly desirable.

In this work we address the above questions by studying the localization properties of a 1D non-Hermitian quasiperiodic model with \mathcal{PT} symmetry [see Eq. (1)], which reduces to the Hermitian t_1 - t_2 model [17–20] when the non-Hermitian parameter is turned off. We show that the ME in this model can be determined analytically by the Sarnak method [63]. This result is remarkable, because the exact ME in the Hermitian t_1 - t_2 model is not yet known. While the spectrum of the Hermitian t_1 - t_2 model contains a hierarchy of gaps, that of the non-Hermitian t_1 - t_2 model is gapless. In fact, the Sarnak method can help us analytically determine the entire spectrum of localized states. These two features make the non-Hermitian t_1 - t_2 model fundamentally different from its Hermitian counterpart. Further, we demonstrate that the

*xiao.li@cityu.edu.hk

metal-insulator transition in this model must occur simultaneously with the spontaneous \mathcal{PT} symmetry breaking transition. Further, we are able to determine exactly the range of the quasiperiodic potential $V_{c1} \leq V \leq V_{c2}$ for which an ME exists in the energy spectrum and also give the expressions for V_{c1} and V_{c2} analytically. Finally, we propose an experimental protocol based on a 1D photonic lattice to distinguish extended and localized states in this model.

II. THE MODEL

To begin with, consider the following non-Hermitian quasiperiodic model,

$$H = \sum_j (t_1 c_j^\dagger c_{j+1} + t_2 c_j^\dagger c_{j+2} + \text{H.c.}) + \sum_j V_j n_j. \quad (1)$$

In the above equation, c_j annihilates a fermion on site j , and $n_j = c_j^\dagger c_j$ counts the particle number on site j . For convenience, we set the hopping strength $t_1 = 1$ as the unit of energy. In addition, we only consider the cases with $t_2 > 0$, as the $t_2 < 0$ can be easily reduced to the $t_2 > 0$ case (see Appendix A for a detailed discussion). The potential energy in Eq. (1) is given by $V_j = V e^{i(2\pi j\alpha + \phi)}$ with $V > 0$. Here we only discuss the $\phi = 0$ case. For results with a general ϕ , please refer to Appendix A. Finally, we take $\alpha = (\sqrt{5} - 1)/2$, which can be approximated by Fibonacci numbers F_n [64,65]: $\alpha = \lim_{n \rightarrow \infty} F_{n-1}/F_n$. Specifically, in our simulations we choose a specific integer n so that the system size is $L = F_n$ and $\alpha = F_{n-1}/F_n$. This choice ensures the \mathcal{PT} symmetry in our model, as shown in Appendix A.

A. The localization transition and ME

As one of the key results in this work, we find that the model in Eq. (1) possesses an energy-dependent ME, given exactly by the following analytical expression:

$$V = \frac{1}{4} |1 + \sqrt{\Delta} + \sqrt{(1 + \sqrt{\Delta})^2 - 16t_2^2}|, \quad (2)$$

where $\Delta = 1 + 4t_2 E + 8t_2^2$, and $E \in [2t_2 - 2, 2t_2 + 2]$ specifies the range of energies at which an ME can exist.¹ As we show below, this ME marks the simultaneous metal-insulator transition and the spontaneous \mathcal{PT} -symmetry breaking transition in this model. In fact, we can use the Sarnak method [63] (see Appendix A for a brief introduction to this method) to derive an analytical condition for the spectrum of localized states in this model, given by

$$\ln |V| = G(E), \quad (3)$$

where $G(E)$ is defined as (see also Appendix A)

$$G(E) = \frac{1}{2\pi} \int_0^{2\pi} \ln |E - 2 \cos \theta - 2t_2 \cos 2\theta| d\theta. \quad (4)$$

The ME condition in Eq. (2) can be viewed as a special case of Eq. (3) when $E \in [2t_2 - 2, 2t_2 + 2]$.

One convenient tool to identify localized states is the inverse participation ratio (IPR), defined as $\text{IPR}(m) =$

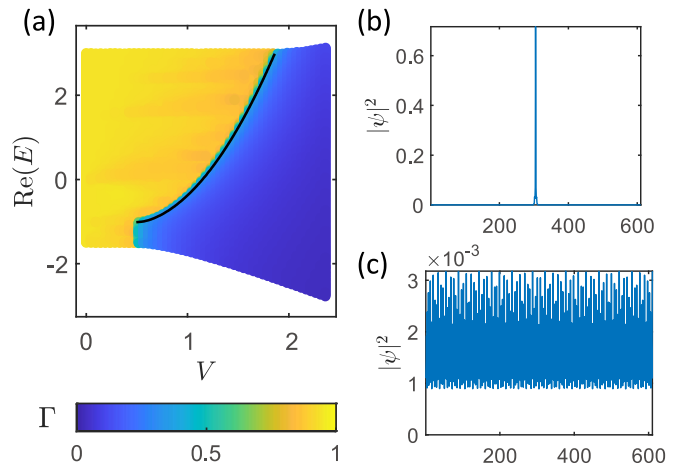


FIG. 1. (a) The fractal dimension Γ as a function of $\text{Re}(E)$ and V in a lattice with size $L = F_{14} = 610$. The black line represents the ME condition in Eq. (2). (b) and (c) plot the wave function for the two states at $V = (V_{c1} + V_{c2})/2$, which has the smallest and largest $\text{Re}(E)$, respectively. Here we choose $t_2 = 1/2$ for all three figures.

$\sum_j |\psi_{m,j}|^4$ [4,27], where m labels the eigenstates and j labels lattice sites. Based on this, we can further introduce the fractal dimension of the wave function, $\Gamma = -\lim_{L \rightarrow \infty} \frac{\ln(\text{IPR})}{\ln L}$. One can show that for extended states $\Gamma \rightarrow 1$, while for localized states, $\Gamma \rightarrow 0$. In Fig. 1(a), we plot the fractal dimension Γ of each eigenstate as a function of $\text{Re}(E)$ and V . In addition, the black line represents the ME condition in Eq. (2). As expected, Γ approaches zero and one for energies on opposite sides of the black line, respectively. This can be further confirmed by the spatial density profile of the respective eigenstates, see Figs. 1(b) and 1(c). In other words, a given eigenstate is localized or extended depends on whether its eigenvalue satisfies $\ln |V| \leq G(\text{Re}(E))$ or $\ln |V| > G(\text{Re}(E))$ (see Appendix A for a proof).

We can thus identify three distinct regimes in Fig. 1(a): for $V < V_{c1}$ ($V > V_{c2}$), the energy spectrum only contains extended (localized) eigenstates, while for $V_{c1} \leq V \leq V_{c2}$, an energy-dependent ME emerges. We will thus denote the regime $V_{c1} \leq V \leq V_{c2}$ as the intermediate phase, since both extended and localized states exist in the spectrum. More importantly, we find that an intermediate phase always exists when $t_2 \neq 0$, and that the exact expressions for V_{c1} and V_{c2} are given by (see Appendix A for the derivation)

$$V_{c1} = \begin{cases} t_2, & t_2 \geq 1/4 \\ \frac{1}{2}(\sqrt{1 - 4t_2} + 1 - 2t_2), & 0 \leq t_2 < 1/4. \end{cases} \quad (5)$$

$$V_{c2} = \frac{1}{2}(\sqrt{1 + 4t_2} + 1 + 2t_2),$$

which are plotted in Fig. 2(a).

Interestingly, Fig. 2(a) shows a curious cusp in V_{c1} at $t_2 = 1/4$, which implies that $t_2 \leq 1/4$ and $t_2 > 1/4$ are two different regimes. This conjecture is confirmed in Figs. 2(b)–2(c), where we plot the ME for $t_2 = 1$ and $t_2 = 1/4$, respectively. We find that when $t_2 > 1/4$ [Fig. 2(b)], the number of localized states suddenly becomes finite as V crosses V_{c1} . In contrast, when $t_2 \leq 1/4$ [Fig. 2(c)], the number of the localized

¹The energy spectrum is guaranteed to be real at the ME.

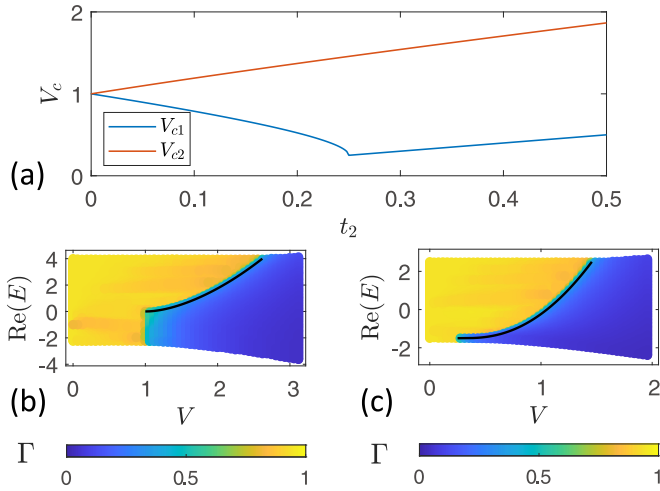


FIG. 2. (a) The boundaries of the intermediate phase as a function of t_2 . V_{c1} and V_{c2} denote the critical V at which the intermediate phase starts and ends for a specific t_2 , see Eq. (5). [(b) and (c)] Fractal dimension Γ of each eigenstate for $t_2 = 1$ and $t_2 = 1/4$, respectively. The black lines represent the ME described by Eq. (2). Here the system size is $L = 610$.

states increases continuously from zero as V crosses V_{c1} . Therefore we conclude that the structure of the ME is qualitatively different when $t_2 \leq 1/4$ and $t_2 > 1/4$.

B. The \mathcal{PT} -symmetry breaking transition

Apart from the metal-insulator transition described above, another interesting property of a \mathcal{PT} -symmetric non-Hermitian model is that this symmetry can be spontaneously broken when the non-Hermitian parameter V exceeds a critical value. Moreover, it is known that this phase transition is accompanied by the transition from an entirely real spectrum to a complex one [60–62]. To demonstrate this property in our model, we keep $t_2 = 1/2$ and plot in Fig. 3 the spectrum for V around V_{c1} and V_{c2} , respectively. The results show that the analytical condition in Eq. (3) (shown as red lines in Fig. 3) correctly captures the spectrum of localized states. In addition, we can observe two different transitions. First, as V increases beyond V_{c1} , complex energies start to emerge from a purely real spectrum, which is accompanied by the appearance of localized states. Second, as V further increases beyond V_{c2} , the spectrum turns into a purely complex one and no extended states exist anymore. The existence of a spontaneous \mathcal{PT} symmetry breaking transition may not be surprising on its own right. What is particularly interesting about our model is that the seemingly unrelated metal-insulator transition occurs simultaneously with this spontaneous \mathcal{PT} symmetry breaking transition. In fact, we can prove this statement rigorously, which is shown in Appendix A.

III. EXPERIMENTAL REALIZATIONS

We now present a realistic experimental realization of the non-Hermitian t_1 - t_2 model in Eq. (1) using a photonic lattice. Such photonic lattices have been routinely used to demonstrate Anderson localization of light [66,67]. A schematic

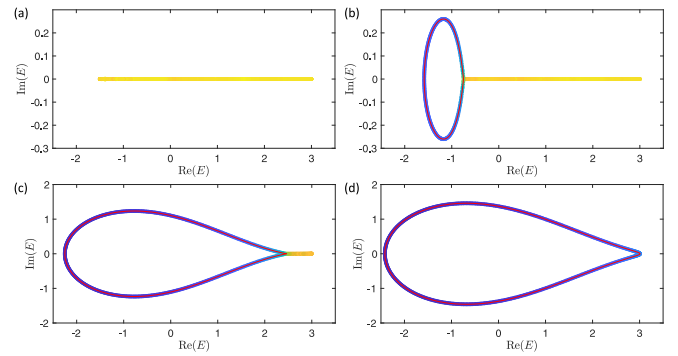


FIG. 3. The complex energy spectrum for (a) $V = V_{c1} - 0.1$, (b) $V_{c1} + 0.3$, (c) $V_{c2} - 0.1$, and (d) $V_{c2} + 0.1$. The color of the energy spectrum represents the fractal dimension Γ of the eigenstates using the same color scale as that in Fig. 1. In addition, the red lines in (b) and (d) (which overlap almost exactly with the numerical results) map out the spectrum of localized states for the corresponding V [see Eq. (3)]. Here we fixed the system size to be $L = 610$, and keep $t_2 = 1/2$.

setup of our proposal is shown in Fig. 4(a). It is known that in the paraxial limit the propagation of classical light in a waveguide can be captured by a form of Maxwell equation that formally resembles the Schrödinger equation in quantum mechanics [68] (see also Appendix B for a discussion). If we further consider the limit in which the light is strongly confined by the waveguides, one can adopt the tight-binding approximation, and cast the continuum wave equation in the following form [68],

$$i \frac{d\psi_j}{dz} = \kappa_j \psi_j + \sum_{l \neq j} J_{j,l} \psi_l. \quad (6)$$

Here the wave vector κ_j is controlled by the refractive index contrast of the j th waveguide and the background medium, while the tunneling parameters $J_{j,l}$ are determined by the overlap between the evanescent tails of the eigenmodes in the j th and l th waveguides [68].

Our model in Eq. (1) can be realized in such a coupled waveguide system where the refractive index in the j th waveguide plays the role of potential V_j and the temporal coordinate t is replaced by the spatial coordinate z . In this work, we choose a system of $L = 21$ coupled waveguides, see Fig. 4(a). In particular, it is possible to engineer the refractive indices of the waveguides so that their real and imaginary parts resemble the complex potential as plotted in Fig. 4(b). We further set $J_{j,j+1} = J_{j,j-1} = t_1$, $J_{j,j+2} = J_{j,j-2} = t_2$, and all other $J_{j,l} = 0$. Further, the waveguides are arranged in a zigzag shape, so under an appropriate arrangement the nearest-neighbor coupling t_1 can be made larger than the next-nearest-neighbor coupling t_2 . In this geometry the ratio t_2/t_1 can be tuned by the angle θ of the zigzag chain, see the inset of Fig. 4(a). Finally, periodic boundary conditions are preferred in the setup.

The localization property of this model can be probed by studying the light propagation in this coupled waveguide system. Here we choose to excite the waveguide at $j = 0$ at $t = 0$, and study how the light spreads out during the propagation.

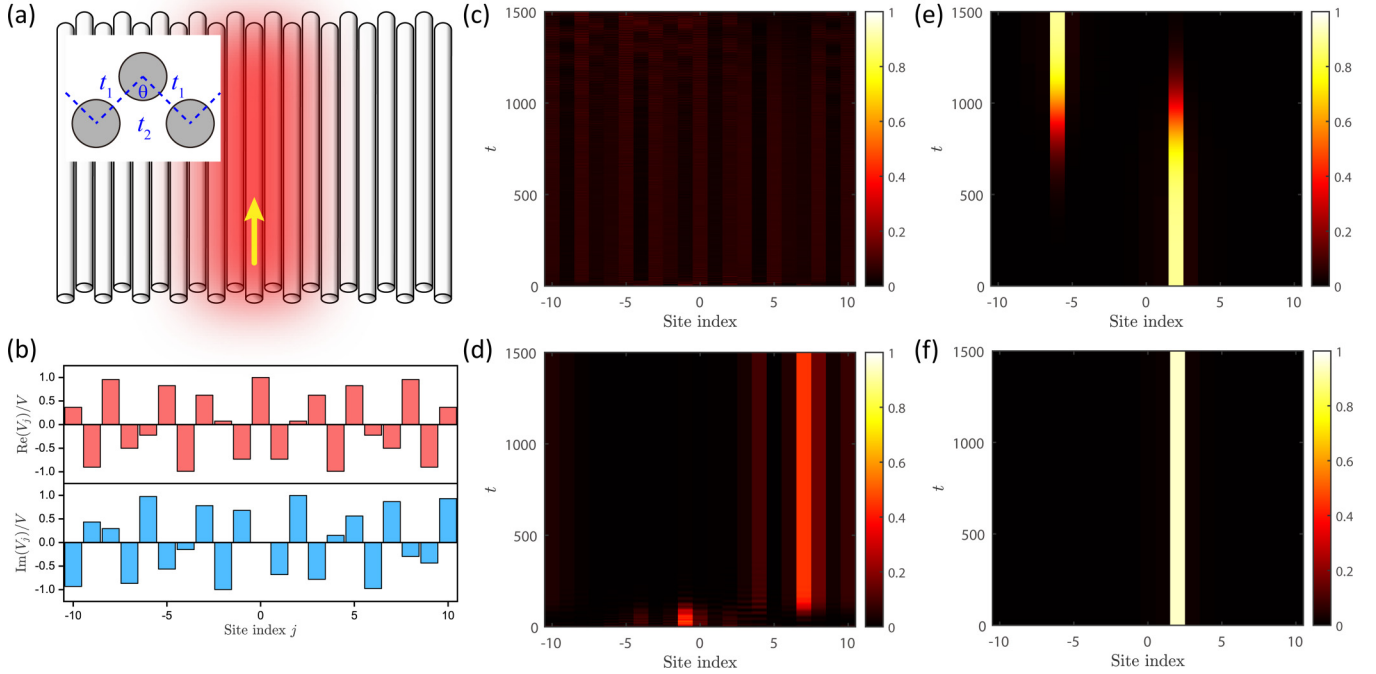


FIG. 4. A realistic experimental realization of the non-Hermitian t_1 - t_2 model in Eq. (1). (a) The schematic setup of a coupled waveguide system consisting of $L = 21$ waveguides. The inset illustrates the coupling between them. Note that the ratio t_2/t_1 can be tuned by varying the angle θ . The arrow indicates that the initial excitation occurs in the $j = 0$ waveguide. (b) A plot of the onsite potential V_j in this coupled waveguide system. The red and blue bars illustrate the real and imaginary part of the potential, respectively. (c)–(f) show the quench dynamics starting from an initial excitation in the $j = 0$ waveguide for $V = V_{c1} - 0.1$, $V_{c1} + 0.3$, $V_{c2} + 1$, $V_{c2} + 2$, respectively. In this plot we choose $\alpha = 13/21$ and $t_2/t_1 = 1/2$. The color bars in (c)–(f) plot the $\bar{n}_j(t)$ defined in Eq. (8). The unit of time is $\tau = \hbar/t_1$. The short-time behavior of $\bar{n}_j(t)$ can be found in Appendix B.

Effectively, we are evaluating

$$|\psi(t)\rangle = e^{-iHt}|\psi_0\rangle = \sum_j e^{-iE_j t} c_j |E_j\rangle, \quad (7)$$

where $|E_j\rangle$ is the j th eigenstate of the Hamiltonian H in Eq. (1) with an energy E_j , and $\{c_j\}$ are the superposition coefficients. The spatial extent of the time evolved state $|\psi(t)\rangle$ can be quantified by

$$\bar{n}_j(t) \equiv \frac{|\langle w_j | \psi(t) \rangle|^2}{\langle \psi(t) | \psi(t) \rangle}, \quad (8)$$

where $|w_j\rangle$ denotes the Wannier function localized within the j th waveguide.

We first consider the $V < V_{c1}$ regime, when all eigenstates in the system are extended. Consequently, we expect that almost all $\bar{n}_j(t)$ are nonzero at late times. In addition, because the spectrum is completely real, all the phase factors $e^{-iE_j t}$ satisfy $|e^{-iE_j t}| = 1$ at all times. As a result, all eigenstates will continue to contribute to the dynamics even when t is large. Our expectations are verified by the results in Fig. 4(c), where we numerically plot $\bar{n}_j(t)$ when $V = V_{c1} - 0.1$. In particular, we find that within a short time the initial excitation spreads out to other waveguides, and $\bar{n}_j(t)$ is almost evenly distributed among all waveguides.

In contrast, when the energy spectrum is complex, the time evolution operator e^{-iHt} is dominated by the eigenstate whose energy eigenvalue has the largest imaginary part. For

convenience, we denote this special eigenvalue as E_{amp} and the corresponding eigenstate as $|E_{\text{amp}}\rangle$. In order to avoid numerical errors induced by the exponential amplifications in the presence of a complex spectrum, we further replace the original Hamiltonian H by $H' = H - i\gamma$ in our simulations, where $\gamma \equiv \text{Im}(E_{\text{amp}}) > 0$. As a result, the state $|E_{\text{amp}}\rangle$ still dominates the quench dynamics, but its amplitude is preserved throughout the dynamics. In contrast, the amplitude of all the other eigenstates decays exponentially. Furthermore, since in this model all states with a complex energy eigenvalue are localized, we anticipate that the final state will be localized whenever the spectrum contains complex energies. In Fig. 4(d), we plot $\bar{n}_j(t)$ for $V = V_{c1} + 0.3$, when the system is in the intermediate phase. We indeed find that the final state is localized. However, in contrast to the quench dynamics in a Hermitian system, the final state is not localized on the original waveguide at $j = 0$, but collapses into the waveguide at $j = 7$. Moreover, we find a curious “jumping process” during the dynamics. Specifically, the initial excitation in the $j = 0$ waveguide almost instantly jumps to a signal peaked at the $j = -1$ waveguide, as shown in Appendix B. At around $t = 100$, this signal jumps again to one localized in the $j = 7$ waveguide. During the entire quench dynamics, the maximum magnitude of $\bar{n}_j(t)$ reaches about 0.4. We also find that the localization length of the final steady state is still quite large, as weak signals with $\bar{n}_j(t) \sim 0.2$ can still be seen in the neighboring waveguides at $j = 4$ and $j = 10$. The above observations show that localization in a non-Hermitian system

is qualitatively different from that in Hermitian systems, and a similar behavior has been reported in a recent work [51]. In particular, the jumping behavior can never occur in a Hermitian system.

In addition, in Figs. 4(e) and 4(f), we plot $\bar{n}_j(t)$ for two different $V > V_{c2}$, when the system is in the localized phase. We find that the qualitative features of Fig. 4(d), especially the jumping behavior, are preserved. For example, in Fig. 4(e), we find that the initial excitation in the $j = 0$ waveguide quickly gives way to an excitation confined in the $j = 2$ waveguide, before eventually collapsing into the waveguide at $j = -6$. In comparison, in Fig. 4(f), we find that the initial excitation in the $j = 0$ waveguide quickly collapses into the waveguide at $j = 2$ and no additional jumps take place afterwards. The main differences between the localized regime and the intermediate regime seem to be quantitative. For example, the localization length of the final steady state is now reduced to just one lattice site. Moreover, the peak value of $\bar{n}_j(t)$ now reaches about 0.8 for Fig. 4(e) and about 0.9 for Fig. 4(f), respectively. It turns out that the curious jumping behavior of $\bar{n}_j(t)$ found in Figs. 4(d)–4(f) arise because there exist several eigenstates whose eigenvalues have similar imaginary parts. In Appendix B, we show that the jumping behavior is a result of the competitions between these eigenstates.

IV. DISCUSSION AND OUTLOOK

Our work represents one of the first examples where the ME in the non-Hermitian quasiperiodic model cannot be directly inferred from its Hermitian counterpart. Indeed, while the exact ME in the Hermitian t_1 - t_2 model is not yet known, we are able to determine the exact ME in our model. In addition, the method developed in this work is very general and can be applied to a wide class of quasiperiodic models. For example, an exact ME can still be obtained when t_2 is complex or when more remote hopping terms are included, which is analyzed in Appendix C. Our work thus not only proposes a realistic experimental scheme to demonstrate ME in a non-Hermitian quasiperiodic model, but also presents a general framework to study other 1D non-Hermitian quasiperiodic models. One important open question is the effect of interactions on the localization properties of this model [69,70]. In particular, it is interesting to understand whether the interplay between interactions and the ME can lead to a many-body intermediate phase [71–73] in this non-Hermitian system.

ACKNOWLEDGMENTS

X.X. is supported by NanKai Zhide Foundation. S.W. acknowledges support from the Research Grants Council of the Hong Kong Special Administrative Region, China (Project Nos. C6013-18G and CityU 11301820). X.L. acknowledges support from the National Natural Science Foundation of China (Grant No. 11904305), the Research Grants Council of the Hong Kong Special Administrative Region, China (Grant No. CityU 21304720 and CityU 11300421), as well as City University of Hong Kong (Project No. 9610428).

APPENDIX A: ADDITIONAL DETAILS OF THE ME

In this section, we provide additional details of the ME for the model we discussed in the main text, which we reproduce here:

$$H = \sum_j (t_1 c_j^\dagger c_{j+1} + t_2 c_j^\dagger c_{j+2} + \text{H.c.}) + \sum_j V_j n_j, \quad (\text{A1})$$

where $V_j = V e^{i(2\pi j\alpha + \phi)}$ with $V > 0$.

1. The \mathcal{PT} symmetry in this model

We first discuss how to ensure an exact \mathcal{PT} symmetry in this model. Note that the parity operator satisfies $\mathcal{P}c_j\mathcal{P} = c_{-j}$, where the site index j is congruent modulo L . Meanwhile, since we are working with a spinless model, the time reversal operator is just taking complex conjugate. As a result, we have

$$\begin{aligned} \mathcal{PT} \left(\sum_{j=0}^{L-1} e^{2\pi i \alpha j} n_j \right) (\mathcal{PT})^{-1} \\ = n_0 + \sum_{j=1}^{L-1} e^{-2\pi i \alpha j} n_{L-j} = n_0 + e^{-2\pi i \alpha L} \sum_{j=1}^{L-1} e^{2\pi i \alpha j} n_j. \end{aligned} \quad (\text{A2})$$

To make assure an exact \mathcal{PT} symmetry, we need αL to be an integer, which is achieved by taking $L = F_n$ and $\alpha = F_{n-1}/F_n$.

2. How does the sign of t_2 affect the spectrum?

In the main text, we only consider the case of $t_2 > 0$. We now explain how the $t_2 < 0$ case is connected to the $t_2 > 0$ case. Equivalently, we can introduce

$$H_{-t_2} = \sum_j [(t_1 c_j^\dagger c_{j+1} - t_2 c_j^\dagger c_{j+2} + \text{H.c.}) + V_j n_j], \quad (\text{A3})$$

where $V_j = V e^{i(2\pi j\alpha + \phi)}$ with $V > 0$. We just need to show how the spectrum of $H_{-t_2}(\phi)$ relates to that of $H(\phi)$ in Eq. (A1). Note that we will explicitly display the global phase ϕ of the potential V_j in each Hamiltonian in this subsection.

First of all, we mention that according to the Sarnak's method, the spectrum of $H(\phi)$ in Eq. (A1) is exactly the same as that of $-H_{-t_2}(\phi)$ in Eq. (A3) in the $L \rightarrow \infty$ limit. To see this, we just need to consider the characteristic functions $G_+(E)$ for $H(\phi)$ and $G_-(E)$ for $H_{-t_2}(\phi)$, as each function completely determines the respective spectrum. Their explicit expressions are given by [see Eq. (A9) below]

$$\begin{aligned} G_+(E) &= \frac{1}{2\pi} \int_0^{2\pi} \ln |E - 2 \cos \theta - 2t_2 \cos 2\theta d| d\theta, \\ G_-(E) &= \frac{1}{2\pi} \int_0^{2\pi} \ln |E - 2 \cos \theta + 2t_2 \cos 2\theta| d\theta. \end{aligned}$$

Hence, we have

$$\begin{aligned} G_+(-E) &= \frac{1}{2\pi} \int_0^{2\pi} \ln |E + 2 \cos \theta + 2t_2 \cos 2\theta| d\theta \\ &= \frac{1}{2\pi} \int_0^{2\pi} \ln |E + 2 \cos(\theta + \pi) \\ &\quad + 2t_2 \cos(2\theta + 2\pi)| d\theta \end{aligned}$$

$$\begin{aligned} &= \frac{1}{2\pi} \int_0^{2\pi} \ln |E - 2 \cos \theta + 2t_2 \cos 2\theta| d\theta \\ &= G_-(E), \end{aligned} \quad (\text{A4})$$

which proves that the spectrum of $H(\phi)$ and that of $H_{-t_2}(\phi)$ just differ by a minus sign.

In a finite system, however, the spectrum of H and H_{-t_2} are connected in a more subtle way. To show this, we introduce the chirality operator \mathcal{C} , which satisfies $\mathcal{C}c_j\mathcal{C}^{-1} = (-1)^j c_j$. As a result, we have

$$\begin{aligned} \mathcal{C}H_{-t_2}(\phi)\mathcal{C}^{-1} &= \sum_j [(-t_1 c_j^\dagger c_{j+1} - t_2 c_j^\dagger c_{j+2} + \text{H.c.}) + Ve^{i(2\pi\alpha j + \phi)} n_j] \\ &= - \sum_j [(t_1 c_j^\dagger c_{j+1} + t_2 c_j^\dagger c_{j+2} + \text{H.c.}) + Ve^{i(2\pi\alpha j + \phi + \pi)} n_j] = -H(\phi + \pi), \end{aligned} \quad (\text{A5})$$

This means that chirality transformation maps $H_{-t_2}(\phi)$ to $-H(\phi + \pi)$.² Therefore, even in a finite system, the $t_2 < 0$ case can always be reduced to the $t_2 > 0$ case. This justifies our choice of $t_2 > 0$ in the main text. Notably, the above result in Eq. (A5) also indicates that the ground state of $H_{-t_2}(\phi)$ will map to the highest-energy state of $H(\phi + \pi)$ and vice versa. As a result, if the ground state of $H(\phi)$ is localized while the highest-energy state is extended [that is, when an ME is present in the spectrum of $H(\phi)$], this transformation (which amounts to flipping the sign of t_2 while keeping t_1 invariant) will turn a localized ground state into an extended one. The fact that the sign of t_2 (the next-nearest-neighbor hopping) can alter the localization property of the ground state of a frustrated lattice model is a well-known effect in the literature [29,74].

The remaining question is, how can we reconcile the finite system result in Eq. (A5) with the infinite-system result in Eq. (A4)? It turns out that for any $0 < \theta < 2\pi$ the spectral difference between $H(\phi)$ and $H(\phi + \theta)$ vanishes in the $L \rightarrow \infty$ limit. To show this, note that we can advance the phase of the potential by $2\pi\alpha m$ through a translation of the system by m sites (since we are dealing with periodic boundary conditions). Moreover, since α is irrational, for any phase difference θ in the potential, there is always an integer $0 < m < L$ that satisfies $2\pi\alpha m - \theta = \mathcal{O}(1/L) \pmod{2\pi}$. Consequently, if T_m denotes the operator that translates the system by m sites, we have

$$\begin{aligned} &\|T_m H(\phi) T_m^{-1} - H(\phi + \theta)\| \\ &= \left\| (e^{2\pi\alpha i m} - e^{i\theta}) \sum_j V e^{2\pi\alpha i j} n_j \right\| = \mathcal{O}(V/L). \end{aligned} \quad (\text{A6})$$

²This transformation is always exact under an open boundary condition (OBC). Under a periodic boundary condition (PBC), however, the above transformation is only exact for an even L . For an odd L with PBC, the mapping has an error of $\mathcal{O}(1/L)$.

Therefore the difference between the spectral norm of $H(\phi)$ and that of $H(\phi + \theta)$ is on the order of $\mathcal{O}(V/L)$, which vanishes in the $L \rightarrow \infty$ limit.

3. More details on the $G(E)$ function

In order to derive the exact ME in our model, we first introduce the following function:

$$f(\theta) = \sum_{j \in \mathbb{Z}} \psi_j e^{ij\theta} \in L^2(\mathbb{T}). \quad (\text{A7})$$

After Fourier transform, which is multiplying Eq. (A1) by $e^{ij\theta}$ and then summing over j , we get the operator

$$Ve^{i\phi} f(\theta + 2\pi\alpha) = [E - 2 \cos \theta - 2t_2 \cos 2\theta] f(\theta), \quad (\text{A8})$$

It has been proved that the spectrum of such a system can be captured by a characteristic function defined as [63]

$$G(E) = \frac{1}{2\pi} \int_0^{2\pi} \ln |E - 2 \cos \theta - 2t_2 \cos 2\theta| d\theta. \quad (\text{A9})$$

Note that we always have $G(E) \geq G(\text{Re}(E))$, because for any $g(\theta) \in \mathbb{R}$, we have

$$\begin{aligned} \ln |E - g(\theta)| &\equiv \ln |\text{Re}(E) + i\text{Im}(E) - g(\theta)| \\ &\geq \ln |\text{Re}(E) - g(\theta)|. \end{aligned}$$

As a result, if we take $g(\theta) = 2 \cos \theta + 2t_2 \cos 2\theta$, we have

$$\begin{aligned} G(E) &= \frac{1}{2\pi} \int_0^{2\pi} \ln |E - g(\theta)| d\theta \\ &\geq \frac{1}{2\pi} \int_0^{2\pi} \ln |\text{Re}(E) - g(\theta)| d\theta \equiv G(\text{Re}(E)). \end{aligned}$$

The Sarnak method [63] then states that the spectrum is determined by the relation between $G(E)$ and $\ln |Ve^{i\phi}| = \ln V$: (1) there is no spectrum within $G(E) < \ln V$; (2) $G(E) = \ln V$ has a dense localized spectrum; and (3) extended states belong to $\{G(E) > \ln V\} \cap U_E$, where U_E is the set of energies that satisfy $E = 2 \cos(\theta) + 2t_2 \cos(2\theta)$ for some θ .

In particular, we can write

$$U_E = \begin{cases} [-1/(4t_2) - 2t_2, 2t_2 + 2], & t_2 \geq 1/4 \\ [2t_2 - 2, 2t_2 + 2], & 0 \leq t_2 < 1/4 \end{cases}$$

After some algebra, we find that

$$G(E) = \ln t_2 + \ln |z_1 \operatorname{sgn}(\operatorname{Re} z_1) + \sqrt{z_1^2 - 1}| + \ln |z_2 \operatorname{sgn}(\operatorname{Re} z_2) + \sqrt{z_2^2 - 1}|, \quad (\text{A10})$$

where $\operatorname{sgn}(x)$ is the sign of the real number x , \sqrt{z} is the square root of z with non-negative real part. In addition, $z_1 = \frac{1}{4t_2}(1 + \sqrt{\Delta})$, $z_2 = \frac{1}{4t_2}(1 - \sqrt{\Delta})$, with $\Delta = 1 + 4t_2E + 8t_2^2$. As a result, $G(E)$ always reaches its minimum value at $E = 2t_2 - 2$, which belongs to U_E . Likewise, $G(E)$ always reaches its maximum value in U_E at $E = 2t_2 + 2$.

4. The expression for V_{c1} and V_{c2}

From the above results, we can determine the structure of the metal-insulator transition in this model, which is accompanied by a \mathcal{PT} symmetry breaking transition in the energy spectrum. In particular, we can introduce two critical points to describe this transition:

$$V_{c1} = e^{G(2t_2-2)} \quad (\text{A11})$$

$$= \begin{cases} t_2, & t_2 \geq 1/4 \\ \frac{1}{2}(\sqrt{1-4t_2} + 1 - 2t_2), & 0 \leq t_2 < 1/4. \end{cases}$$

$$V_{c2} = e^{G(2t_2+2)} = \frac{1}{2}[2t_2 + 1 + \sqrt{4t_2 + 1}]. \quad (\text{A12})$$

These two points divide the phase diagram into three regimes. For $V < V_{c1}$, all eigenstates are extended. Meanwhile, the energy spectrum resides in U_E and is thus entirely real. For $V_{c1} < V < V_{c2}$, an ME appears in the energy spectrum, indicating that extended and localized eigenstates coexist in the energy spectrum. Meanwhile, we observe that the spectrum contains both real and complex eigenvalues. Finally, when $V > V_{c2}$, we have $G(E) < \ln |V|$ for all $E \in U_E$, and thus the entire spectrum is localized and complex in general.

5. Localization transition and the \mathcal{PT} symmetry breaking transition

In fact, we can prove rigorously that in our model [Eq. (A1)] the \mathcal{PT} symmetry breaking transition (which is signaled by the real-complex transition in the energy spectrum) and the localization transition must occur simultaneously. First we note that extended spectrum must be real, since $U_E \subset \mathbb{R}$. Therefore we just need to prove localized states must have complex energy eigenvalues. However, there is a subtlety here, as few localized states still have real energy eigenvalues. In particular, the following localized states are known to have real eigenvalues: (1) all eigenstates on the ME (marked by the solid black line in Fig. 5) and (2) eigenstates at the boundary of the spectrum (marked by dashed black lines in Fig. 5). However, given that they are all located at the boundary of the spectrum of localized states, they do not affect our claim that the \mathcal{PT} symmetry transition must be accompanied by the metal-insulator transition in this model.

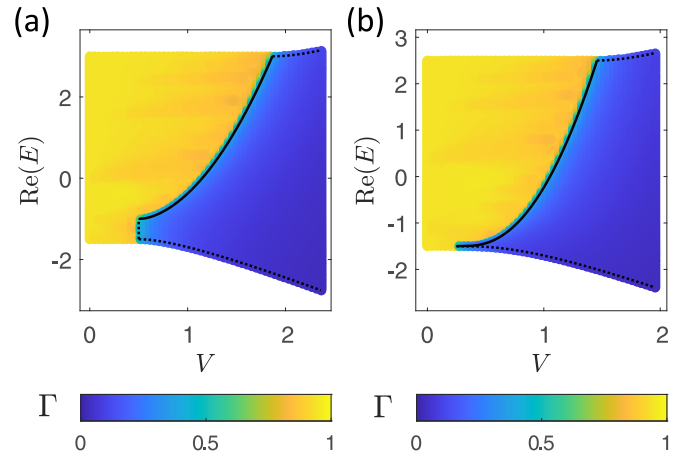


FIG. 5. (a) and (b) show the fractal dimension Γ of each eigenstate for the model in Eq. (A1) for $t_2 = 1/2$ and $1/4$, respectively. The system size is $L = 610$. The solid black line highlights eigenstates on the ME (which are localized states with a real energy eigenvalue), while the dashed black lines highlight additional localized states with a real energy eigenvalue.

We now show that apart from those marked by the solid and the dashed black lines in Fig. 5, all other localized eigenstates (which occur for $V > V_{c1}$) have complex energy eigenvalues. To start, consider the real part of the complex spectrum

$$\mathcal{M} = \{\operatorname{Re}(E) : G(E) = \ln V \text{ \& \; } \operatorname{Im}(E) \neq 0\}.$$

As we pointed out below Eq. (A9), $G(E) \geq G(\operatorname{Re}(E))$ for all E . As a result, we must have $\mathcal{M} \subset \mathcal{M}'$, where

$$\mathcal{M}' = \{x \in \mathbb{R} : G(x) < \ln V\}.$$

We can see clearly that \mathcal{M}' is a nonempty open set in \mathbb{R} , since at least $2t_2 - 2 \in \mathcal{M}'$. To see this, note that we are considering $V > V_{c1}$, and hence $\ln V > \ln V_{c1} = G(2t_2 - 2)$, leading to $2t_2 - 2 \in \mathbb{R}$. We further note that $G(E) \rightarrow +\infty$ as $|E| \rightarrow +\infty$. Therefore, due to the continuity of $G(E)$, for any real number $E \in \mathcal{M}'$, there always exists a complex number E' that satisfies the following conditions:

$$\operatorname{Re}(E') = E \text{ \& \; } G(E') = \ln V.$$

Consequently, we obtain $\mathcal{M} = \mathcal{M}'$. Therefore the real localized spectrum is just the boundary of the open set \mathcal{M}' , while every point inside \mathcal{M}' corresponds to at least one complex localized state, which proves our statement.

Besides, from the above analysis, we know that if E is an eigenvalue, then the statement that the state $|E\rangle$ is extended is equivalent to $G(\operatorname{Re}(E)) > \ln V$. Similarly, the statement that $|E\rangle$ is localized is equivalent to the condition that $G(\operatorname{Re}(E)) \leq \ln V$.

6. The t_2 transition

Additionally, another property of $G(E)$ is that $G(E)$ is a constant function on the interval $[-1/(4t_2) - 2t_2, 2]$, which implies that when $t_2 \geq 1/4$ there are a bunch of E reaching the minimum of $G(E)$. As a result, multiple eigenstates will be localized simultaneously as $\ln(V)$ reaches V_{c1} . This property explains the difference between panels (b) and (c)

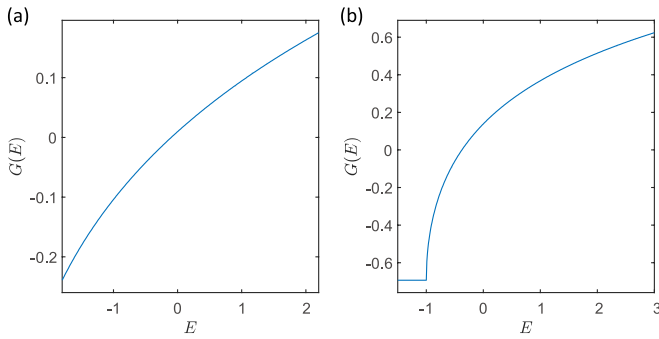


FIG. 6. (a) and (b) plot $G(E)$ in Eq. (A9) with $t_2 = 0.1$ and $t_2 = 0.5$ on U_E , respectively. The set of energies on these two curves satisfying $G(E) > \ln V$ belongs to extended states.

in Fig. 2 in the main text. One such example is shown in Fig. 6, which plots $G(E)$ on U_E for two different values of t_2 . In particular, for a given V , all points on the curve satisfying $G(E) > \ln V$ correspond to extended states in the system. Specifically, when $0 < t_2 < 1/4$ the $G(E) \cap U_E$ is a monotonic curve, and hence the number of localized states increases continuously from zero at $V = V_{c1}$. In contrast, when $t_2 > 1/4$ the $G(E) \cap U_E$ has a plateau. As a result, the number of localized states is already finite at $V = V_{c1}$.

7. The IPR and NPR in this model

One of the most widely used tools to diagnose the existence of ME is to plot the averaged inverse participation ratio (IPR) and normalized participation ratio (NPR) of all eigenstates [23,27]. In particular, these two quantities are defined as

$$\text{IPR}^{(i)} = \sum_n |u_n^{(i)}|^4, \quad \text{NPR}^{(i)} = \left[L \sum_n |u_n^{(i)}|^4 \right]^{-1}.$$

In the above equation, L is the size of the one-dimensional system, the index i labels different eigenstates, while the index n labels different lattice sites. We will use IPR and NPR to denote the averaged IPR and NPR over all single-particle eigenstates, respectively.

It is known that when the spectrum contains only extended states, we have $\text{IPR} \sim L^{-1}$ while NPR is finite. In contrast, when the spectrum contains only localized states we have $\text{NPR} \sim L^{-1}$ while IPR is finite. Only when the spectrum contains both extended and localized states, both IPR and NPR are finite.

A plot of IPR and NPR for $t_2 = 1/2$ is shown in Fig. 7. We can see that the intermediate phase indeed appears for $V_{c1} < V < V_{c2}$, where $V_{c1} = 1/2$ and $V_{c2} = 1 + \sqrt{3}/2$ for $t_2 = 1/2$. It is interesting to note that the IPR is almost constant in the extended phase ($0 < V < V_{c1}$) for this non-Hermitian model, indicating that the localization length of the eigenstates does not decrease much when V is increased from 0 to V_{c1} . In contrast, for a Hermitian quasiperiodic model, there is a clear decrease of IPR in the extended phase as V increases from 0 to V_{c1} [23,27]. However, currently we do not fully understand the reason behind this difference.

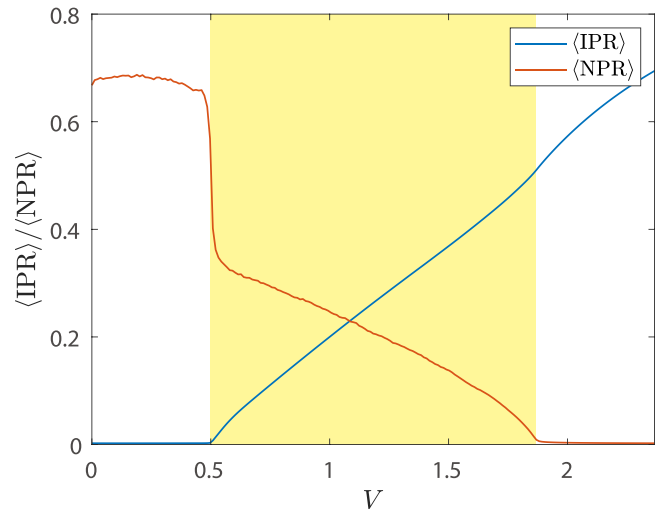


FIG. 7. IPR and NPR for the model in Eq. (A1) with $t_2 = 1/2$. The yellow background highlights the region when both extended and localized states appear in the energy spectrum.

APPENDIX B: FURTHER DETAILS ON THE EXPERIMENTAL PROPOSAL

In this section, we provide additional details on the experimental proposal in Fig. 4 in the main text.

1. The long-time dynamics

We first focus on the long-time behavior of the system, and discuss the switching behavior observed in Fig. 4 in the main text.

We first discuss panel (e) of Fig. 4 in the main text, which corresponds to $V = V_{c2} + 1$. In this case the state $|E_{\text{amp}}\rangle$ is localized around the $j = -6$ waveguide. Meanwhile, the eigenvalue of the state localized around the $j = 2$ waveguide has an imaginary part that is only slightly smaller. Such a result can be seen in Fig. 8(a). Consequently, the waveguide at $j = 2$ quickly takes over the initial excitation, because it is much closer to the initially excited waveguide (at $j = 0$) than the waveguide at $j = -6$. However, the state $|E_{\text{amp}}\rangle$ eventually dominates the dynamics at long times, and the excitation finally collapses onto the waveguide at $j = -6$.

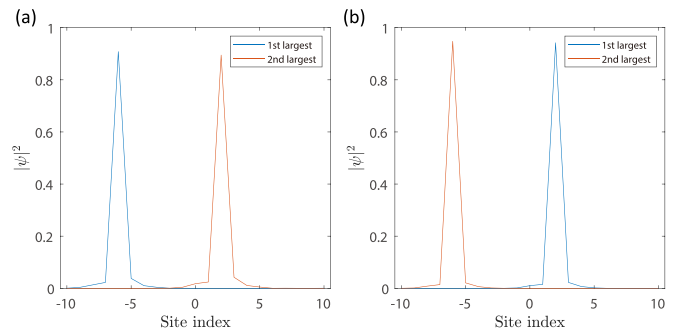


FIG. 8. The two eigenstates with the largest imaginary energies in an $L = 21$ system for the model in Eq. (A1). In particular, the blue line corresponds to the state $|E_{\text{amp}}\rangle$ defined in the text. (a) and (b) show the results with $V = V_{c2} + 1$ and $V = V_{c2} + 2$, respectively.

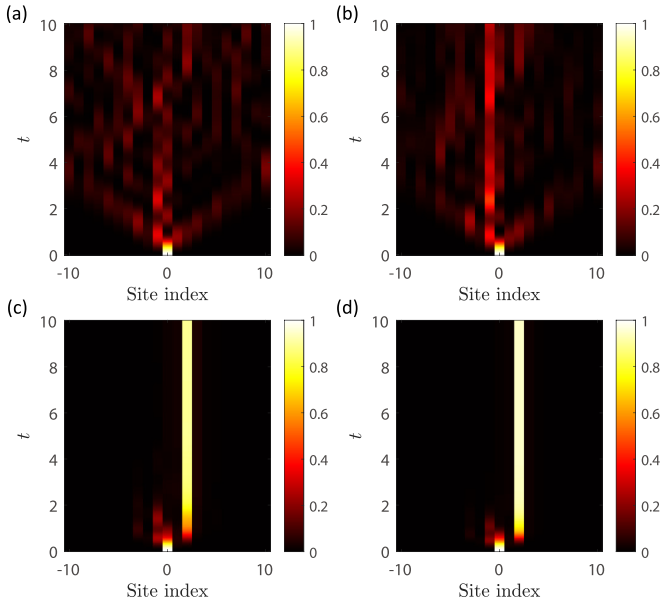


FIG. 9. Short-time behavior of the experimental protocol shown in Fig. 4(a) in the main text. The system consists of $L = 21$ waveguides, which are described by the model in Eq. (A1). (a)–(d) show the quench dynamics starting from an initial excitation in the middle $j = 0$ waveguide for $V = V_{c1} - 0.1$, $V_{c1} + 0.3$, $V_{c2} + 1$, and $V_{c2} + 2$, respectively. The unit of time is $\tau = \hbar/t_1$ in all figures.

In contrast, when $V = V_{c2} + 2$, which corresponds to panel (f) of Fig. 4, the state $|E_{\text{amp}}\rangle$ now resides in the waveguide at $j = 2$, as shown in Fig. 8(b). As a result, the initial excitation quickly collapses onto the waveguide at $j = 2$, and will not switch to other waveguides afterwards. It is also worth noting that the strong localization limit of $V = V_{c2} + 2$ can be understood directly from the potential distribution in Fig. 4(b) in the main text, because all eigenstates are well approximated by the Wannier functions in this limit, and the eigenvalues are also close to the potential energies in each waveguide. As we can see from Fig. 4(b) in the main text, $\text{Im}(V_{j=2})$ is indeed the largest among all, while $\text{Im}(V_{j=-6})$ is a close second. This is the fundamental reason why the dynamics in the strong localization limit is dominated by these two waveguides.

2. The short-time dynamics

Having understood the long-time dynamics, we now discuss the short-time behavior of the quench dynamics, which is shown in Fig. 9. First, we observe that the initial excitation at $j = 0$ was only retained in the system for less than $t = \tau$ in all four cases, where $\tau = \hbar/t_1$ is a natural unit of time in our model. Second, in the presence of extended states ($V < V_{c2}$), the signal quickly spreads out to all waveguides. In particular, a light-cone-like structure is clearly visible, as shown in Figs. 9(a) and 9(b). In contrast, when the spectrum contains localized states only ($V > V_{c2}$), the light-cone-like structure is gone. Instead, the initial excitation switches between different waveguides during the time evolution, and the exact dynamical process depends on the structure of the energy spectrum. For example, in Fig. 9(c), when $\tau < t < 2\tau$ the light propagates in the form of a state with appreciable

amplitudes on the $j = -3$, $j = -1$, and $j = 2$ waveguides. However, when $t > 2\tau$ the amplitudes in the $j = -3$ and $j = -1$ waveguides gradually die off, and only the $j = 2$ waveguide has an appreciable amplitude. The behavior in Fig. 9(d) is similar to that in (c), although the amplitude in the $j = 2$ waveguide is much stronger when $t > 2\tau$.

APPENDIX C: THE CASE OF COMPLEX HOPPING PARAMETERS

In order to illustrate the versatility of our method, in this section, we show that we can derive the exact ME condition even when both t_1 and t_2 are complex. This extension also has direct experimental applications because in photonic lattices it is possible to generate complex hoppings between neighboring waveguides. Specifically, we consider the following Hamiltonian,

$$H = \sum_j (t_1 e^{i\phi_1} c_j^\dagger c_{j+1} + t_2 e^{i\phi_2} c_j^\dagger c_{j+2} + \text{H.c.}) + \sum_j V_j n_j.$$

In the above equation, the two phases can be reduced to one independent parameter $\phi_2 - 2\phi_1$ by the substitution $c_j^\dagger \rightarrow e^{-i\phi_1 j} c_j^\dagger$. As a result, we shall consider the following Hamiltonian instead

$$\tilde{H} = \sum_j (c_j^\dagger c_{j+1} + \tilde{t}_2 c_j^\dagger c_{j+2} + V_j n_j + \text{H.c.}), \quad (\text{C1})$$

where we have defined $\tilde{t}_2 = t_2 e^{i\phi}$ with $\phi = \phi_2 - 2\phi_1$. Note that we again set $t_1 = 1$ and $t_2 > 0$, in accordance with our convention in the main text.

To proceed, we now apply the Fourier transformation in Eq. (A7) to rewrite Eq. (C1) in terms of $f(\theta)$ as

$$V f(\theta + \alpha) = [E - 2 \cos \theta - 2t_2 \cos(2\theta - \phi)] f(\theta).$$

Correspondingly, the function $G(E)$ and the set U_E are defined respectively as

$$G(E) = \frac{1}{2\pi} \int_0^{2\pi} \ln |E - g(\theta)| d\theta, \quad (\text{C2})$$

$$U_E = \{E : \exists \theta, \text{ s.t. } E = g(\theta)\}, \quad (\text{C3})$$

where $g(\theta) \equiv 2 \cos \theta + 2t_2 \cos(2\theta - \phi)$.

1. An exact expression for $G(E)$

For the present model, we can still derive an analytic expression for $G(E)$:

$$\begin{aligned} G(E) &= \frac{1}{2\pi} \int_0^{2\pi} \ln |E - 2 \cos \theta - 2t_2 \cos(2\theta - \phi)| d\theta \\ &= \frac{1}{2\pi} \oint_{|z|=1} \ln |z + 1/z + \tilde{t}_2 z^2 + \tilde{t}_2^*/z^2 - E| \frac{dz}{iz} \\ &= \frac{1}{2\pi} \oint_{|z|=1} \ln |\tilde{t}_2 z^4 + z^3 - E z^2 + z + \tilde{t}_2^*| \frac{dz}{iz} \\ &= \ln t_2 + \sum_{k=1}^4 \frac{1}{2\pi} \oint_{|z|=1} \ln |z - z_k| \frac{dz}{iz}, \end{aligned} \quad (\text{C4})$$

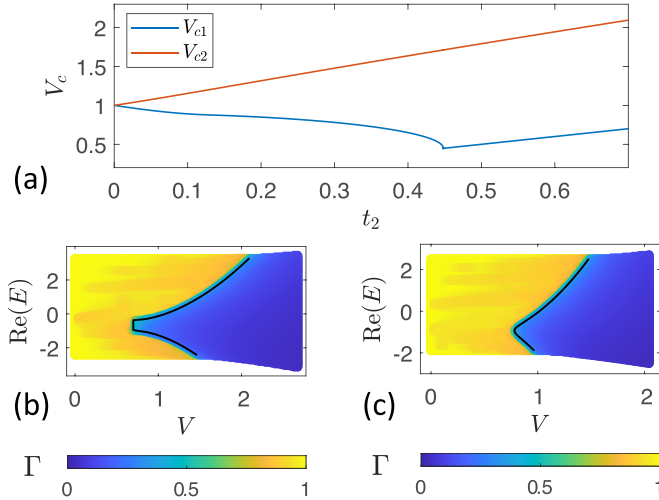


FIG. 10. (a) plots the two transition points V_{c1}, V_{c2} with respect to t_2 obtained numerically. (b) and (c) plot $t_2 = 0.7$ and $t_2 = 0.3$ respectively. The color of (b) and (c) represents the fractal dimension of the eigenstates and the black lines are derived numerically from $G(E) = \ln |V|$. Finally, $\phi_2 - 2\phi_1 = \pi/4$ in all three figures and the system size is $L = 610$.

where z_k are the four roots of the following equation:

$$\tilde{t}_2 z^4 + z^3 - E z^2 + z + \tilde{t}_2^* = 0. \quad (\text{C5})$$

If we further note that

$$\frac{1}{2\pi} \oint_{|z|=1} \ln |z - z'| \frac{dz}{iz} = \begin{cases} \ln |z'|, & |z'| \geq 1 \\ 0, & |z'| < 1 \end{cases} \quad (\text{C6})$$

we find that

$$e^{G(E)} = t_2 \prod_{k=1}^4 \max(|z_k|, 1), \quad (\text{C7})$$

which satisfies $e^{G(E)} \geq t_2$. Because z_k are just the roots of a quartic equation, they can still be written in closed forms. Besides, when $\phi = 0$, we can substantially simplify z_k by the following relation

$$\begin{aligned} 0 &= z + 1/z + t_2 z^2 + t_2/z^2 - E \\ &= (z + 1/z) + t_2(z + 1/z)^2 - (E + 2t_2), \end{aligned} \quad (\text{C8})$$

which can be used to derive Eq. (A10).

In Figs. 10(b) and 10(c), we compare the predicted ME in Eq. (C7) with the single-particle spectrum in a finite system.

In particular, we choose $\phi = \pi/4$ and study two cases with $t_2 = 0.7$ and $t_2 = 0.3$, respectively. We find that our theoretical predictions of the ME (black solid line) agrees well with the numerical results.

2. An exact expression for $t_2^{(c)}$

Another interesting observation from Fig. 10(a) is that the structure of the ME is again different for small t_2 and large t_2 , although the critical point now shifts to $t_2 \approx 0.45$ instead of $1/4$ for the $\phi = 0$ case. We now show that this critical $t_2^{(c)}$ can again be determined analytically. This can be done without writing down z_k explicitly.

To begin with, note from Eq. (C5) that we have $z_1 z_2 z_3 z_4 = \tilde{t}_2^*/\tilde{t}_2$, which implies that

$$\sum_{k=1}^4 \ln |z_k| = \ln |\tilde{t}_2^*/\tilde{t}_2| = 0. \quad (\text{C9})$$

As a result, we note from Eq. (C7) that

$$G(E) = \sum_{k=1}^4 \max(\ln |z_k|, 0) + \ln t_2 \quad (\text{C10})$$

$$= \frac{1}{2} \sum_{k=1}^4 |\ln |z_k|| + \ln t_2 \geq \ln t_2. \quad (\text{C11})$$

Hence, the last equality holds if and only if all four roots satisfy $|z_k| = 1$.

We know that $V_{c1} = \min e^{G(E)}$, so if there exists an energy E that allows such four roots, then $V_{c1} = t_2$, independent of ϕ . Besides, if there are more than one such E , they all turn into localized states at once as V passes t_2 . Hence, to determine the critical t_2 , we need to check whether Eq. (C5) allows four roots on $|z| = 1$ for some E . Equivalently, we can ask whether the equation $E = 2 \cos \theta + 2t_2 \cos(2\theta - \phi)$ allows four roots in a period for some E . This condition amounts to ask whether $2 \sin \theta + 2t_2 \sin(2\theta - \phi) = 0$ has four roots. Based on this observation, we can derive the expression for the critical point $t_2^{(c)}$ as follows:

$$t_2^{(c)}(\phi) = \frac{1}{4} \left[\left| \sin \frac{\phi}{2} \right|^{2/3} + \left| \cos \frac{\phi}{2} \right|^{2/3} \right]^{3/2}. \quad (\text{C12})$$

In particular, when $\phi = \pi/4$, we have $t_2^{(c)} \approx 0.448$, in agreement with the observation in Fig. 10(a).

[1] P. W. Anderson, *Phys. Rev.* **109**, 1492 (1958).
 [2] E. Abrahams, P. W. Anderson, D. C. Licciardello, and T. V. Ramakrishnan, *Phys. Rev. Lett.* **42**, 673 (1979).
 [3] P. A. Lee and T. V. Ramakrishnan, *Rev. Mod. Phys.* **57**, 287 (1985).
 [4] F. Evers and A. D. Mirlin, *Rev. Mod. Phys.* **80**, 1355 (2008).
 [5] M. Schreiber, S. S. Hodgman, P. Bordia, H. P. Lüschen, M. H. Fischer, R. Vosk, E. Altman, U. Schneider, and I. Bloch, *Science* **349**, 842 (2015).
 [6] P. Bordia, H. P. Lüschen, S. S. Hodgman, M. Schreiber, I. Bloch, and U. Schneider, *Phys. Rev. Lett.* **116**, 140401 (2016).

[7] J. y. Choi, S. Hild, J. Zeiher, P. Schauss, A. Rubio-Abadal, T. Yefsah, V. Khemani, D. A. Huse, I. Bloch, and C. Gross, *Science* **352**, 1547 (2016).
 [8] H. P. Lüschen, P. Bordia, S. S. Hodgman, M. Schreiber, S. Sarkar, A. J. Daley, M. H. Fischer, E. Altman, I. Bloch, and U. Schneider, *Phys. Rev. X* **7**, 011034 (2017).
 [9] H. P. Lüschen, P. Bordia, S. Scherg, F. Alet, E. Altman, U. Schneider, and I. Bloch, *Phys. Rev. Lett.* **119**, 260401 (2017).
 [10] P. Bordia, H. Lüschen, S. Scherg, S. Gopalakrishnan, M. Knap, U. Schneider, and I. Bloch, *Phys. Rev. X* **7**, 041047 (2017).

- [11] D. A. Abanin, E. Altman, I. Bloch, and M. Serbyn, *Rev. Mod. Phys.* **91**, 021001 (2019).
- [12] C. M. Soukoulis and E. N. Economou, *Phys. Rev. Lett.* **48**, 1043 (1982).
- [13] S. Das Sarma, A. Kobayashi, and R. E. Prange, *Phys. Rev. Lett.* **56**, 1280 (1986).
- [14] S. Das Sarma, S. He, and X. C. Xie, *Phys. Rev. Lett.* **61**, 2144 (1988).
- [15] D. J. Thouless, *Phys. Rev. Lett.* **61**, 2141 (1988).
- [16] S. Das Sarma, S. He, and X. C. Xie, *Phys. Rev. B* **41**, 5544 (1990).
- [17] J. Biddle, B. Wang, D. J. Priour, and S. Das Sarma, *Phys. Rev. A* **80**, 021603(R) (2009).
- [18] J. Biddle and S. Das Sarma, *Phys. Rev. Lett.* **104**, 070601 (2010).
- [19] J. Biddle, D. J. Priour, B. Wang, and S. Das Sarma, *Phys. Rev. B* **83**, 075105 (2011).
- [20] R. Ramakumar, A. Das, and S. Sil, *Physica A* **401**, 214 (2014).
- [21] S. Ganeshan, J. H. Pixley, and S. Das Sarma, *Phys. Rev. Lett.* **114**, 146601 (2015).
- [22] X. Deng, S. Ray, S. Sinha, G. V. Shlyapnikov, and L. Santos, *Phys. Rev. Lett.* **123**, 025301 (2019).
- [23] X. Li and S. Das Sarma, *Phys. Rev. B* **101**, 064203 (2020).
- [24] Y. Wang, X. Xia, L. Zhang, H. Yao, S. Chen, J. You, Q. Zhou, and X.-J. Liu, *Phys. Rev. Lett.* **125**, 196604 (2020).
- [25] Z. Xu, H. Huangfu, Y. Zhang, and S. Chen, *New J. Phys.* **22**, 013036 (2020).
- [26] S. Roy, T. Mishra, B. Tanatar, and S. Basu, *Phys. Rev. Lett.* **126**, 106803 (2021).
- [27] X. Li, X.-P. Li, and S. Das Sarma, *Phys. Rev. B* **96**, 085119 (2017).
- [28] H. P. Lüschen, S. Scherg, T. Kohlert, M. Schreiber, P. Bordia, X. Li, S. Das Sarma, and I. Bloch, *Phys. Rev. Lett.* **120**, 160404 (2018).
- [29] F. A. An, E. J. Meier, and B. Gadway, *Phys. Rev. X* **8**, 031045 (2018).
- [30] T. Kohlert, S. Scherg, X. Li, H. P. Lüschen, S. Das Sarma, I. Bloch, and M. Aidelsburger, *Phys. Rev. Lett.* **122**, 170403 (2019).
- [31] V. Goblot, A. Štrkalj, N. Pernet, J. L. Lado, C. Dorow, A. Lemaître, L. L. Gratiet, A. Harouri, I. Sagnes, S. Ravets, A. Amo, J. Bloch, and O. Zilberberg, *Nat. Phys.* **16**, 832 (2020).
- [32] F. A. An, K. Padavić, E. J. Meier, S. Hegde, S. Ganeshan, J. H. Pixley, S. Vishveshwara, and B. Gadway, *Phys. Rev. Lett.* **126**, 040603 (2021).
- [33] N. Hatano and D. R. Nelson, *Phys. Rev. Lett.* **77**, 570 (1996).
- [34] N. Hatano and D. R. Nelson, *Phys. Rev. B* **56**, 8651 (1997).
- [35] N. Hatano and D. R. Nelson, *Phys. Rev. B* **58**, 8384 (1998).
- [36] J. Feinberg and A. Zee, *Phys. Rev. E* **59**, 6433 (1999).
- [37] A. Jazaeri and I. I. Satija, *Phys. Rev. E* **63**, 036222 (2001).
- [38] L. G. Molinari, *J. Phys. A: Math. Theor.* **42**, 265204 (2009).
- [39] D. M. Jović, C. Denz, and M. R. Belić, *Opt. Lett.* **37**, 4455 (2012).
- [40] C. Yuce, *Phys. Lett. A* **378**, 2024 (2014).
- [41] C. H. Liang, D. D. Scott, and Y. N. Joglekar, *Phys. Rev. A* **89**, 030102(R) (2014).
- [42] C. Mejía-Cortés and M. I. Molina, *Phys. Rev. A* **91**, 033815 (2015).
- [43] A. Amir, N. Hatano, and D. R. Nelson, *Phys. Rev. E* **93**, 042310 (2016).
- [44] A. K. Harter, T. E. Lee, and Y. N. Joglekar, *Phys. Rev. A* **93**, 062101 (2016).
- [45] S. Longhi, *Phys. Rev. Lett.* **122**, 237601 (2019).
- [46] A. F. Tzortzakakis, K. G. Makris, and E. N. Economou, *Phys. Rev. B* **101**, 014202 (2020).
- [47] Y. Huang and B. I. Shklovskii, *Phys. Rev. B* **101**, 014204 (2020).
- [48] Q.-B. Zeng, Y.-B. Yang, and Y. Xu, *Phys. Rev. B* **101**, 020201(R) (2020).
- [49] Z. Xu and S. Chen, *Phys. Rev. A* **103**, 043325 (2021).
- [50] F. L. Metz and I. Neri, *Phys. Rev. Lett.* **126**, 040604 (2021).
- [51] A. F. Tzortzakakis, K. G. Makris, A. Szameit, and E. N. Economou, *Phys. Rev. Research* **3**, 013208 (2021).
- [52] Q.-B. Zeng, S. Chen, and R. Lü, *Phys. Rev. A* **95**, 062118 (2017).
- [53] S. Longhi, *Phys. Rev. B* **100**, 125157 (2019).
- [54] Y. Liu, X.-P. Jiang, J. Cao, and S. Chen, *Phys. Rev. B* **101**, 174205 (2020).
- [55] T. Liu, H. Guo, Y. Pu, and S. Longhi, *Phys. Rev. B* **102**, 024205 (2020).
- [56] Q.-B. Zeng and Y. Xu, *Phys. Rev. Research* **2**, 033052 (2020).
- [57] Y. Liu, Y. Wang, X.-J. Liu, Q. Zhou, and S. Chen, *Phys. Rev. B* **103**, 014203 (2021).
- [58] S. Longhi, *Phys. Rev. B* **103**, 144202 (2021).
- [59] Y. Liu, Y. Wang, Z. Zheng, and S. Chen, *Phys. Rev. B* **103**, 134208 (2021).
- [60] C. M. Bender and S. Boettcher, *Phys. Rev. Lett.* **80**, 5243 (1998).
- [61] C. M. Bender, *Rep. Prog. Phys.* **70**, 947 (2007).
- [62] R. El-Ganainy, K. G. Makris, M. Khajavikhan, Z. H. Musslimani, S. Rotter, and D. N. Christodoulides, *Nat. Phys.* **14**, 11 (2018).
- [63] P. Sarnak, *Commun. Math. Phys.* **84**, 377 (1982).
- [64] M. Kohmoto, *Phys. Rev. Lett.* **51**, 1198 (1983).
- [65] Y. Wang, Y. Wang, and S. Chen, *Eur. Phys. J. B* **89**, 254 (2016).
- [66] T. Schwartz, G. Bartal, S. Fishman, and M. Segev, *Nature (London)* **446**, 52 (2007).
- [67] Y. Lahini, A. Avidan, F. Pozzi, M. Sorel, R. Morandotti, D. N. Christodoulides, and Y. Silberberg, *Phys. Rev. Lett.* **100**, 013906 (2008).
- [68] T. Ozawa, H. M. Price, A. Amo, N. Goldman, M. Hafezi, L. Lu, M. C. Rechtsman, D. Schuster, J. Simon, O. Zilberberg, and I. Carusotto, *Rev. Mod. Phys.* **91**, 015006 (2019).
- [69] R. Hamazaki, K. Kawabata, and M. Ueda, *Phys. Rev. Lett.* **123**, 090603 (2019).
- [70] L.-J. Zhai, S. Yin, and G.-Y. Huang, *Phys. Rev. B* **102**, 064206 (2020).
- [71] Y.-T. Hsu, X. Li, D.-L. Deng, and S. Das Sarma, *Phys. Rev. Lett.* **121**, 245701 (2018).
- [72] S. Xu, X. Li, Y.-T. Hsu, B. Swingle, and S. Das Sarma, *Phys. Rev. Research* **1**, 032039(R) (2019).
- [73] Y. Wang, C. Cheng, X.-J. Liu, and D. Yu, *Phys. Rev. Lett.* **126**, 080602 (2021).
- [74] T. Mishra, R. V. Pai, S. Mukerjee, and A. Paramekanti, *Phys. Rev. B* **87**, 174504 (2013).